JAAS

PAPER

Cite this: *J. Anal. At. Spectrom.*, 2017, **32**, 385

Structure of the Fe and Ni L X-ray spectra

A. Sepúlveda,[a] T. Rodríguez,[a] P. D. Pérez,[a] A. P. L. Bertol,[b] A. C. Carreras,[a] J. Trincavelli,[a] M. A. Z. Vasconcellos,[b] R. Hinrichs[c] and G. Castellano*[a]

Received 2nd November 2016
Accepted 9th December 2016

DOI: 10.1039/c6ja00398b

www.rsc.org/jaas

Fe-L and Ni-L X-ray spectra induced by electron impact were analyzed. The measurements were made on bulk samples using a commercial wavelength dispersive spectrometer, and the spectra were processed with a parameter optimization method previously developed. This procedure allowed for the determination of characteristic energies, relative transition probabilities and natural linewidths. The results obtained are compared to the data found in the literature, when available. Satellite and radiative Auger emissions were also analyzed, energy shifts and relative intensities being determined. Many of these parameters were determined for the first time, which was possible due to the robustness of the spectral processing method used. The line profile introduced here takes into account the differential attenuation at both sides of the absorption edge.

1 Introduction

A precise knowledge of certain atomic parameters, such as characteristic energies, relative transition probabilities (RTP) and natural linewidths, is the key to give a detailed description of the fundamental processes that govern the interaction of electrons with matter. Any advance in the knowledge of these parameters constitutes a contribution in the field of atomic physics, particularly in the study of relaxation processes. Decays in the presence of a spectator hole give rise to satellite lines, which along with the so called radiative Auger emission (RAE) bands, usually overlap with the diagram lines. These structures need to be taken into account for a reliable analytical description of an X-ray emission spectrum, their study being therefore of practical interest for several spectroscopic techniques. This fact is particularly important for the L lines of transition metals in the fourth period, due to the scarcity of data available in the literature. A reliable method to process the experimental spectra is necessary to face the determination of such parameters. To this end, all the spectral contributions must be taken into account: characteristic peaks, bremsstrahlung continuum, satellite bands or peaks, RAE structures and detection artifacts.

The experimental characteristic energies available for iron and nickel involve measurements performed by Bearden[1] and Cauchois and Sénémaud.[2] On the other hand, theoretical calculations were carried out by Indelicato *et al.*[3] and Deslattes *et al.*[4] for the characteristic energies, and by Scofield[5] for the RTPs. These parameters were also predicted by Perkins *et al.*[6] for all the elements and transitions. Finally, a set of natural linewidths compiled by Campbell and Papp[7] is also available for a large number of transitions.

In this work, the structure of Fe-L and Ni-L X-ray emission spectra induced by electron incidence is analyzed. Relative transition probabilities, characteristic energies and natural linewidths were determined for a number of atomic transitions from L shell vacancy states. In addition, some multiple ionization satellite lines and RAE bands were studied. To achieve these goals, the experimental spectra were processed using a robust fitting procedure based on a method of parameter refinement, which takes into account all the mentioned spectral contributions.[8]

2 Experimental

L-Spectra from pure bulk Fe and Ni samples were measured with a JEOL JXA 8230 microprobe, equipped with a Johansson type wavelength dispersive spectrometer (WDS). The emitted X-rays were diffracted by a TAP analyzing crystal and recorded by a P10 flow counter. All the spectra were induced by a 5 keV incident electron beam and collected at a take-off angle of 40°. The beam currents and acquisition times were respectively 100.8 nA and 256.1 min for Fe, while those for Ni were 102.0 nA and 125.0 min.

2.1 Detection efficiency

For the correct determination of the relative intensities of the peaks and structures present in the spectra, an accurate knowledge of the spectrometer efficiency is necessary. The WDS efficiency depends on parameters that are difficult to know to

[a]*Facultad de Matemática, Astronomía y Física, Universidad Nacional de Córdoba – Instituto de Física Enrique Gaviola, Ciudad Universitaria, 5000, Córdoba, Argentine Republic. E-mail: gcas@famaf.unc.edu.ar*

[b]*Instituto de Física, Universidade Federal do Rio Grande do Sul (UFRGS), Porto Alegre, Rio Grande do Sul, Brazil*

[c]*Instituto de Geociências, Universidade Federal de Rio Grande do Sul, Porto Alegre, Rio Grande do Sul, Brazil*

a reasonable extent; for example, the diffractor crystal reflectivity, the counter sealant window transmissivity, the counter efficiency itself, *etc.* There are different methods to determine the efficiency curve; for instance, it can be derived from the comparison of two measurements of the same bremsstrahlung spectrum acquired with different spectrometers, a WDS and an energy dispersive spectrometer (EDS) of known efficiency.[9] For the present study, instead, characteristic emissions were used, to take advantage of the high statistics involved in the detection processes.

Special care has to be taken when obtaining the photon yield of a peak measured using a WDS, because its channels are not immediately adjacent, unlike an EDS measurement. Fig. 1 displays a scheme for the number of photons $I(E)$ detected between E and $E + \Delta E$, where ΔE is related to the spectrometer resolution and $\overline{\Delta E}$ stands for the energy difference between two successive positions of the analyzing crystal. In an energy dispersive spectrometer $\overline{\Delta E} = \Delta E$, and the intensity yield of a peak is merely assessed by adding the intensities of all channels involved in the peak. In the case of a WDS instead, the intervals are different, so that the total intensity of a measured peak cannot be obtained in the same way: if $\Delta E \geq \overline{\Delta E}$, count overlap would distort the characteristic intensity recorded; if $\Delta E \leq \overline{\Delta E}$, there would be photons not taken into account (between points A and B in Fig. 1, for example). Thus, in a WDS, the adequate assessment of a peak intensity centered in E_q involves the area

$$N_q = \int_{E_q - w}^{E_q + w} I(E)\mathrm{d}E \tag{1}$$

where w is an energy such that the interval between $E_q - w$ and $E_q + w$ covers all the photons emitted by the transition considered. It can be seen that N_q is independent of $\overline{\Delta E}$ for a reasonable choice of this energy step length.[10] It is clear that this integral has energy units and is proportional to the total number of measured characteristic photons P_q.

The effective efficiency ε used in this work is defined as the proportionality factor between the peak area of a characteristic line q and the number of these photons emitted by the sample per incident electron P'_q,

$$\varepsilon(E_q) = \frac{N_q}{n_\mathrm{e} P'_q},$$

where n_e is the number of incident electrons for which the peak area has been measured in the WDS system. It has to be noted that the efficiency defined in this way has energy units because the peak area N_q has also energy units. From this expression, it follows that to determine $\varepsilon(E_q)$, P'_q is required, which can be obtained by using an EDS spectrometer whose efficiency is well established, namely

$$P'_q = \sum_i \frac{P_\mathrm{EDS}(E_i)}{\frac{\Delta\Omega}{4\pi}\varepsilon_\mathrm{int}(E_i)n}, \tag{2}$$

where P_EDS is the number of characteristic photons measured by the spectrometer at energy E_i, n the corresponding number of incident electrons, $\Delta\Omega$ the solid angle subtended by the EDS detector window from the impact point of the electrons on the sample and $\varepsilon_\mathrm{int}(E_i)$ is the intrinsic efficiency at energy E_i. The index i in the summation runs over all the channels comprised by the q line. Thus

$$\varepsilon(E_q) = \frac{N_q}{n_\mathrm{e}}\left(\sum_i \frac{P_\mathrm{EDS}(E_i)}{\frac{\Delta\Omega}{4\pi}\varepsilon_\mathrm{int}(E_i)n}\right)^{-1}. \tag{3}$$

The intrinsic efficiency $\varepsilon_\mathrm{int}(E_i)$ involved in these expressions was determined from the thicknesses of the several layers composing the detector, following the procedure explained in ref. 8. In order to determine the solid angle subtended by the X-ray detector, Monte Carlo simulations were performed by means of the PENCYL example program included in the PENELOPE package.[11] This program was modified to determine the photons emitted by the sample in the take-off angle of 40° with an angular acceptance of ±5°. To maximize statistics minimizing the simulation time, the X-ray emission in all the azimuthal angles was integrated. Several measured bremsstrahlung spectra were compared with their corresponding Monte Carlo simulations in the region between 3 and 6 keV, following the methodology explained in ref. 12, for Si, Zr and Au samples irradiated with 8 keV and 20 keV electrons. The solid angle obtained from the corresponding fitting process was $(1.15 \pm 0.05) \times 10^{-4}$ sr. Fig. 2 displays a comparison between the experimental spectrum of a pure Zr sample at 8 keV and the corresponding simulation scaled with the solid angle obtained.

The value of ε was obtained by measuring the L emission spectra from Cr, Fe, Co, Ni and Cu pure standards. Also, fluorite (CaF_2) and tugtupite ($Na_4AlBe(Si_4O_{12})Cl$) samples were measured in order to obtain respectively the F and Na K emission spectra. The inclusion of all these elements allowed to take into account the entire energy interval of interest in this work (Fe and Ni L spectra). The samples were irradiated with 8 keV electrons and the emitted spectra were measured with both EDS and WDS.

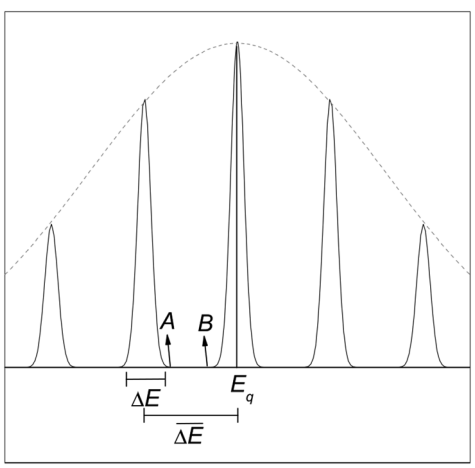

Fig. 1 Scheme depicting the ΔE and $\overline{\Delta E}$ parameters.

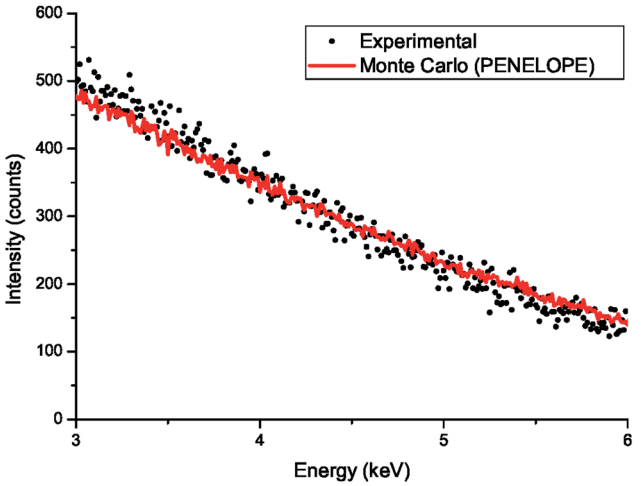

Fig. 2 Experimental 8 keV spectrum and scaled Monte Carlo simulated bremsstrahlung for a pure Zr standard, after fitting the $\Delta\Omega$ for the EDS detector.

Eqn (3) was thus applied to compare the characteristic intensities measured with both spectrometers for these standards. Because of their different resolutions, a peak measured with the EDS may contain several L emissions that are resolved in the WDS measurement. In this work, the Lα and Lβ characteristic intensities, respectively P_α and P_β, registered in the WDS were compared to the EDS intensity for the L group (Lα, Lβ, Lℓ and Lη) according to

$$N_q = P_\alpha\left(1+\frac{p_\ell}{p_\alpha}\right)+P_\beta\left(1+\frac{p_\eta}{p_\beta}\right), \quad (4)$$

where the transition rates p_q were taken from Scofield.[5]

The results for the efficiency and its fitting curve are plotted in Fig. 3, comprising energies between 0.5728 keV (Cr-Lα) and 1.041 keV (Na-Kα). It must be pointed out that this energy interval is almost the entire operation range of the crystal. The efficiency curve obtained allowed to produce adequate fittings for both Fe and Ni spectra, as shown in Fig. 4 and 5. As can be seen, appropriate spectral predictions were achieved in both cases, as reflected by χ^2 values below 1.35.

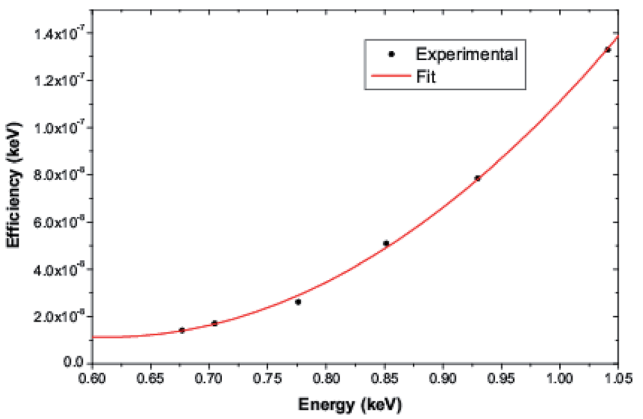

Fig. 3 WDS efficiency curve.

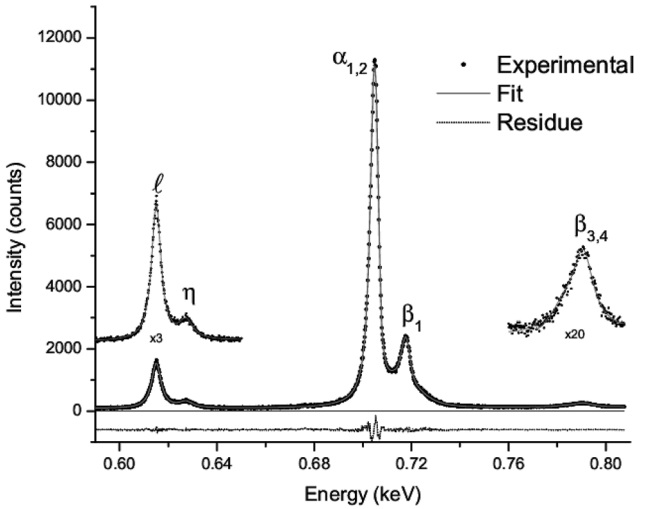

Fig. 4 L-Spectrum of Fe measured at 5 keV. The insets show magnified views of the regions involving weak peaks.

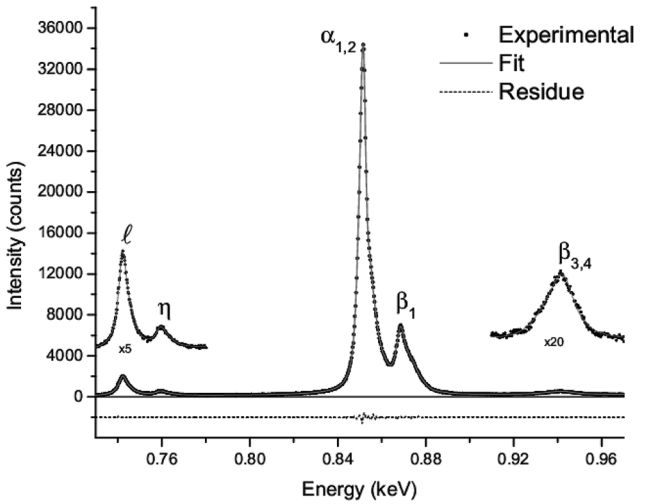

Fig. 5 L-Spectra of Ni measured at 5 keV. The insets show magnified views of the regions involving weak peaks.

3 Spectral analysis

The spectral processing was performed using the software POEMA,[8] which is based on an optimization method of atomic and experimental parameters. This processing involves the fitting of an analytical expression $\bar{I}_i$ which describes the intensity as a function of the energy E_i of channel i, *i.e.*

$$\bar{I}_i = B(E_i)+\sum_q P_q S_q(E_i), \quad (5)$$

where B is the background radiation and S_q is a function accounting for the peak profile. The different choices for the peak profile are described in Subsection 3, whereas the number of photons registered P_q is assessed as

$$P_q = \beta\sigma_\ell^{\chi} p_q (ZAF)_q \varepsilon(E_q), \quad (6)$$

where β is a constant proportional to the number of incident electrons, σ_ℓ^{x} is the X-ray production cross-section for the ℓ subshell, *i.e.*, the product of the final vacancy production cross-section $\tilde{Q}_\ell$ and the fluorescence yield ω_ℓ; p_q is the corresponding relative transition probability and Z and F are the atomic number and fluorescence correction factors, respectively. The absorption correction A is usually considered as a factor independent of E_i; as explained below, in certain cases, variations within a linewidth must be taken into account more carefully, as implemented here by modifying the profiles S_q.

The L-shell final vacancy production cross-sections can be written as

$$\tilde{Q}_{\mathrm{L}_1} = Q_{\mathrm{L}_1},$$

$$\tilde{Q}_{\mathrm{L}_2} = Q_{\mathrm{L}_2} + f_{1,2}Q_{\mathrm{L}_1},$$

$$\tilde{Q}_{\mathrm{L}_3} = Q_{\mathrm{L}_3} + f_{2,3}Q_{\mathrm{L}_2} + (f_{1,3} + f_{1,2}f_{2,3})Q_{\mathrm{L}_1},$$

where Q_ℓ is the ionization cross-section for the ℓ subshell and $f_{k,j}$ is the probability of the Coster–Kronig transition for an initial state with a vacancy in the L_k subshell and a final state with a vacancy in the L_j subshell.

The fitting procedure consists in minimizing the quadratic differences between the experimental spectrum and the analytical function proposed to describe it [eqn (5)] through the optimization of the parameters involved in the analytical function. Thus, the quantity to be minimized is

$$\chi^2 = \frac{1}{N_{\mathrm{c}} - N_{\mathrm{p}}} \sum_{i=1}^{N_{\mathrm{c}}} \frac{(\bar{I}_i - I_i)^2}{I_i}, \tag{7}$$

where I_i and $\bar{I}_i$ are the experimental and predicted intensities, respectively, N_{c} is the number of channels and N_{p} is the number of parameters to be refined. Then, after a sequence of optimization steps, a detailed description of all the spectral features is achieved, and the values of a set of atomic and experimental parameters are obtained. The uncertainties related to the parameters obtained were estimated by propagating the errors of the experimental channel intensities by numerical differentiation.[13] To perform this calculation, all the models involved in the analytical description of the spectrum ($\bar{I}_i$) were assumed to be exact; this approximation is reasonable, since the main contributions to the resulting uncertainties are due to experimental statistical errors, which are more determinant in the case of weak lines.

Although in some cases a spectral fitting can be improved by artificially increasing the number of structures considered, the strategy implemented along this work consisted in maintaining the minimum number of peaks allowing for an acceptable fit. In every case where a transition not previously reported was introduced in the present work, it was clear that the spectrum evidently bears this emission, and consequently the fitting dramatically worsens when this line is omitted.

3.1 Line profiles

In atomic physics, several relative transition probabilities and natural linewidths are related to the lifetime of the corresponding decays. The Voigt function permits to describe the characteristic line profiles in a realistic way, because this function involves a Gaussian contribution $G(E)$ due to instrumental features, and a Lorentzian component $L_q(E)$ intrinsic to the nature of the characteristic line q emission process[14]

$$S_q(E) = \int L_q\left(E'\right) G\left(E - E'\right) \mathrm{d}E', \tag{8}$$

Due to the lack of a closed-form expression for the Voigt function, the pseudo-Voigt approach is often used in X-ray spectroscopy,[15,16] though this linear combination of a Gaussian and a Lorentzian does not properly reflect the nature of the emission–detection process. For this reason, a Voigt profile is used in this work for all the characteristic peaks not very close to an absorption edge, as detailed below. For the RAE bands, instead, a convolution between a Gaussian profile and the expression given by Enkisch[17] was used, thus taking into account the asymmetric shape of these structures.

The characteristic photons are affected by absorption when they leave the sample. In most peaks, the absorption factor $A(E')$ can be considered uniform within the narrow energy interval involved in the linewidth. Instead, special care must be taken when a peak is very close to its corresponding absorption edge, at an energy difference lesser than the spectrometer resolution. In this situation, an important asymmetry can be observed as a noticeable step at the high energy side, due to a differential absorption along the peak,[16] as is the case of Fe- and Ni-L$\alpha_{1,2}$ doublets, where the L_3 absorption edge intercepts the high energy side of the peak. For these cases, the absorption correction modifies the Lorentzian profile shape that reaches the spectrometer, since $A(E')$ can no longer be regarded as a constant. To account for this effect, instead of the empirical approach implemented by Rémond *et al.*,[16] a general strategy was adopted, *i.e.*, eqn (8) was solved by a numerical integration routine involving the absorption correction in the convolution:

$$S_q(E) = \int L_q\left(E'\right) A\left(E'\right) G\left(E - E'\right) \mathrm{d}E'. \tag{9}$$

It is worth noting that with this definition for S_q, the absorption factor in eqn (6) must be excluded, in order not to consider it twice in eqn (5).

4 Results and discussion

4.1 Characteristic energies

All the peaks observed in the spectra were identified as diagram lines, satellite transitions or RAE structures. In Fig. 4 and 5, all the diagram transitions are indicated next to their corresponding peaks. The shoulders appearing close to some of the peaks are due to satellite and RAE structures, which are discussed in Subsection 4.4.

The characteristic energies obtained in this work are presented in Table 1, along with results published by Bearden,[1] Cauchois and Sénémaud[2] and Deslattes *et al.*[4] Since thermal fluctuations are avoided in the laboratory, for the present

Table 1 Characteristic energies (in keV) obtained for Fe and Ni. Numbers in parentheses indicate the estimated uncertainties in the last digits

	Fe				Ni			
Transition	This work	Ref. 1	Ref. 2	Ref. 4	This work	Ref. 1	Ref. 2	Ref. 4
L_3M_1 (ℓ)	0.6150(8)	0.6152(3)	0.61549	0.6170(12)	0.7421(2)	0.7427(4)	0.74238	0.7445(12)
L_2M_1 (η)	0.6273(8)	0.628(1)	0.62777	0.6306(17)	0.7594(3)	0.762(1)	0.75971	0.7622(17)
L_2M_4 (β_1)	0.7176(8)	0.7185(4)	0.71796	0.7211(7)	0.8685(4)	0.8688(4)	0.86824	0.8710(7)
L_1M_2 (β_3)	0.783(4)			0.7872(13)	0.936(3)			0.9391(15)
		0.792(1)	0.79037			0.9410(7)	0.94064	
L_1M_3 (β_4)	0.7906(9)			0.7938(14)	0.9423(9)			0.9443(16)

assessments the spectrometer gain value was taken from the default calibration settings. The spectrometer zero parameter, instead, was fitted so that the energy of the most intense peak ($L_3M_{4,5}$ doublet) matches the value reported by Bearden.[1] To estimate the uncertainty of each transition energy, the fitting error was added in quadrature with the error reported by Bearden for the line taken as reference.

For the comparison of characteristic energies displayed in Fig. 6, in the case of Deslattes *et al.*[4] and the results obtained in this work, the $L_1M_{2,3}$ doublets (as reported by Bearden[1] and Cauchois and Sénémaud[2]) have been assessed by weighted averaging the energy values through the corresponding RTPs reported in Subsection 4.2. Several remarks can be stated from the energy differences displayed in Fig. 6. First of all, the theoretical values[4] appear to overestimate the experimental data from different sources, in about 2–3 eV. Most experimental characteristic energies investigated lie within an interval narrower than 1 eV. For the particular case of the $L_1M_{2,3}$ doublet, it must be pointed out that two lines are evidently present in the spectra for both elements (Fig. 4 and 5), and the two fitted energies are distinguishable in both cases, as displayed in Table 1. In the values reported in ref. 1 and 2, however, one single energy is presented for each element, which suggests that the global spectrum processing methodology used here provides characteristic energy values with a better resolution.

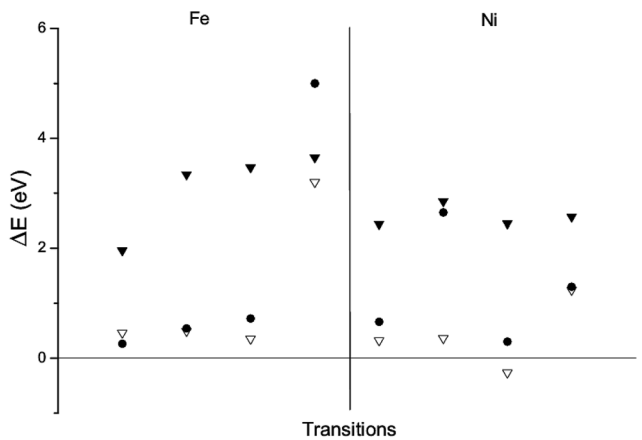

Fig. 6 Differences of the characteristic energies reported by other authors relative to the values obtained in this work. The transitions displayed on the *x* axis are in the same order as in Table 1. Solid circles: ref. 1, open triangles: ref. 2, solid triangles: ref. 4.

4.2 Relative transition probabilities

The RTP corresponding to an L_kX_j line is the probability for this transition relative to all radiative decays to the L_k subshell. Table 2 shows the RTP values obtained in this work, along with the data reported by Scofield[5] and by Perkins *et al.*[6] To normalize the RTPs, all the transitions observed experimentally were taken into account.

As can be seen from Fig. 7, the results published by Perkins *et al.*[6] markedly disagree with the other sets of data shown. In fact, according to these authors, Lα and $L\beta_1$ lines are weaker than $L\ell$ and Lη lines, respectively. A better agreement of the present results with the theoretical data given by Scofield[5] can be seen. Although a noticeable discrepancy for the L_3M_1 line appears, it is clearly smaller than the deviations of the data given by Perkins *et al.* relative to the other sets of data.

4.3 Natural linewidths

As described in Section 3, the peak profile used involves the natural linewidth besides the instrumental broadening γ_G. This instrumental broadening is a function of the photon energy, whose parameters are shared by all peaks and can be derived from Bragg's law, as detailed previously:[18]

$$\gamma_G = \sqrt{2\ln 2}\Delta\theta E\sqrt{\left(\frac{2d}{hc}E\right)^2 - 1} \quad (10)$$

where d is the interplanar spacing of the crystal, h is the Planck constant and c is the speed of light in vacuum. Thus, each peak at energy E can be described by means of two parameters,

Table 2 Relative transition probabilities obtained for Fe and Ni. Numbers in parentheses indicate the estimated uncertainties in the last digits

	Fe			Ni		
Transition	This work	Ref. 5	Ref. 6	This work	Ref. 5	Ref. 6
L_3M_1 (ℓ)	0.1795(11)	0.08636	0.729	0.1200(11)	0.06321	0.577
$L_3M_{4,5}$ ($\alpha_{1,2}$)	0.821(4)	0.9136	0.271	0.880(3)	0.9368	0.423
L_2M_1 (η)	0.105(3)	0.08299	0.742	0.083(2)	0.05989	0.593
L_2M_4 (β_1)	0.90(5)	0.9170	0.258	0.92(4)	0.9401	0.407
L_1M_2 (β_3)	0.45(28)	0.3481	0.402	0.448(18)	0.3481	0.395
L_1M_3 (β_4)	0.55(24)	0.6519	0.598	0.552(15)	0.6519	0.605

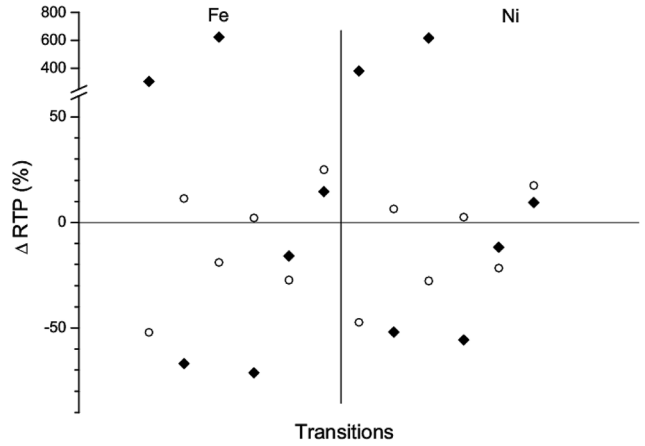

Fig. 7 Percent differences of the RTP data reported by other authors relative to the values obtained in this work. The transitions displayed on the abscissas run in the same order as in Table 2. Open circles: ref. 5, solid diamonds: ref. 6.

refinable with POEMA: its natural linewidth and the angular divergence $\Delta\theta$ of the analyzer crystal—the latter being common to all the peaks present in the spectrum.

Table 3 shows the natural linewidths obtained in this work along with data calculated from the energy level widths published by Perkins *et al.*[6] and by Campbell and Papp.[7] For both cited studies, these linewidths were obtained by adding the widths corresponding to the energy levels involved in each transition. The linewidths for the decays involving M_4 and M_5 subshells cannot be assessed from either of these studies, since these level widths were not reported for Fe and Ni.

It can be seen that there are important discrepancies between the two cited datasets, and also with the linewidths obtained here. In the particular case of the L_1M_2 decay, an apparent overestimation of the linewidth has been produced through the present fit. It must be pointed out, however, that this value for the linewidth cannot be avoided to achieve a correct description of the experimental spectrum. Nevertheless, the linewidths obtained through the level widths recommended by Campbell are based on reliable XPS measurements; on the other hand, the X-ray experimental spectra clearly bear a structure that cannot be explained by means of the mere addition of atomic level widths. A possible explanation might rely on the occurrence of multiplets, *i.e.*, more complex structures caused by atomic level unfolding. In the case of a system with a partly filled 3d band, like Fe and Ni, after an ionization process, the final state will have an incompletely filled 3d band. When the ionization occurs in an s level, multiplet effects are due to the exchange interaction between the spin of the s-core hole and the spin of the valence electrons. This effect is particularly important for s holes higher than 1s for which multiplet effects are larger, implying a splitting of the atomic levels,[19] which, in turn, leads to a splitting in the emission spectrum after the initial vacancy is filled from a more external level.

Table 3 Natural linewidths (in eV) obtained for Fe and Ni. Numbers in parentheses indicate the estimated uncertainties in the last digits

	Fe			Ni		
Trans.	This work	Ref. 6	Ref. 7	This work	Ref. 6	Ref. 7
L_3M_1	4.6(5)	4.11	2.81	3.8(6)	4.78	2.83
$L_3M_{4,5}$	3.8(8)	—	—	2.3(8)	—	—
L_2M_1	7.5(6)	4.1	3.54	4.9(6)	4.78	3.28
L_2M_4	5.0(9)	—	—	4.5(9)	—	—
L_1M_2	19.1(19)	8.89	8.23	19.3(11)	11.1	7.7
L_1M_3	9.4(16)	8.89	8.23	12.2(11)	11.0	7.7

4.4 Satellite lines and radiative Auger emission

Multiple peak structures appearing in experimental X-ray emission spectra can be attributed to different causes. One of them, particularly important in 3d transition metals, involves the overlap of core and valence wave functions, which in the case of an s-core hole is due to the spin exchange interaction between the core hole and the valence electrons, as discussed in the previous subsection. On the other hand, it is well known that multiple ionization can slightly distort the atomic energy levels, giving rise to the so-called spectator hole satellite lines.

All these numerous transitions not always are observable separately due to the natural linewidths involved and because of the finite spectrometer energy resolution. Nevertheless, their joint effect can be phenomenologically described including a reduced number of satellite lines, whose origin may be a mixture of diverse causes.

Inner-shell vacancy states may also relax through radiative Auger emissions, *i.e.*, the final state being a doubly ionized atom accompanied by the emission of an outer electron and an X-ray photon.[18]

In Table 4 the energy shifts and relative areas of satellite bands and RAE structures obtained in this work are summarized. The energy shifts ΔE are defined as the differences between the fitted centroids and the corresponding diagram decay energies; data published by Cauchois and Sénémaud[2] are also included in the table for comparison. Each relative area reported has been assessed as the ratio of the corresponding peak area to the sum of the parent line area and the areas of all the RAEs and satellites arising from it.

It can be seen that the energies assigned to the satellite lines are in good agreement with those reported by Cauchois and Sénémaud,[2] although some minor differences were found. In the case of the satellite lines obtained in this work for iron, only one structure was enough to produce an adequate description of both L_3 and L_2 groups, due to the appropriate line profile implemented here (eqn (9)) to account for the differential attenuation around the absorption edges. In addition, the present results include three new satellite lines for Ni, respectively associated with the L_3M_1, L_2M_1 and L_2M_4 diagram lines.

As detailed elsewhere,[18] when the relaxation energy of an L_iR_j transition is shared between a photon and an Auger electron ejected from the T_k shell, the energy balance leads to:

$$E(L_iR_j) - E_m \gtrsim E(T_k), \quad (11)$$

Table 4 Relative energies and areas of satellite lines and RAE bands

			ΔE (eV)		
	Parent line		This work	Ref. 2	Relative area (%)
Fe	$L_3M_{4,5}$	sat.	7.6	6.5	6.7
				4.3	
	L_2M_4	sat.	5.9	6.5	27.4
				4.3	
Ni	L_3M_1	sat.	2.1		46.1
	$L_3M_{4,5}$	sat.	3.0	4.2	31.9
		sat.	5.8	6.2	13.3
		sat.	9.8	9.2	3.11
		RAE	−1.3		5.75
	L_2M_1	sat.	3.1		42.3
	L_2M_4	sat.	3.2	3.9	21.4
		sat.	6.2	6.7	17.3
		sat.	9.8		6.71

where $E(L_iR_j)$ is the characteristic energy related to the L_iR_j transition, E_m is the energy at the RAE band maximum and $E(T_k)$ stands for the Auger electron binding energy.

From (11), it is always possible to associate a RAE structure found from the spectral processing with a particular absorption edge. According to this criterion, the RAE observed for Ni might be related to the $M_{4,5}$ absorption edge, *i.e.*, to an $L_3M_{4,5}M_{4,5}$ Auger emission. This assignment arises by considering the absorption edge $M_{4,5}$ value 3.6 ± 0.4 eV given by Bearden and Burr,[20] while the ΔE value obtained here is 1.3 eV (see Table 4).

In Fig. 8 and 9 the Lα–Lβ$_1$ region of Fe and Ni spectra is respectively plotted. The fitting curve, as well as diagram line contributions, satellite lines and RAE structures are detailed in the figures. As it can be seen, the Ni spectrum is more complex than the Fe spectrum, and several additional satellite structures are noticeable. When the emission energies are very close to the absorption edge, some of the plotted peaks clearly show (particularly for Fe) the effect of the differential absorption accounted for in the line profile implemented here.

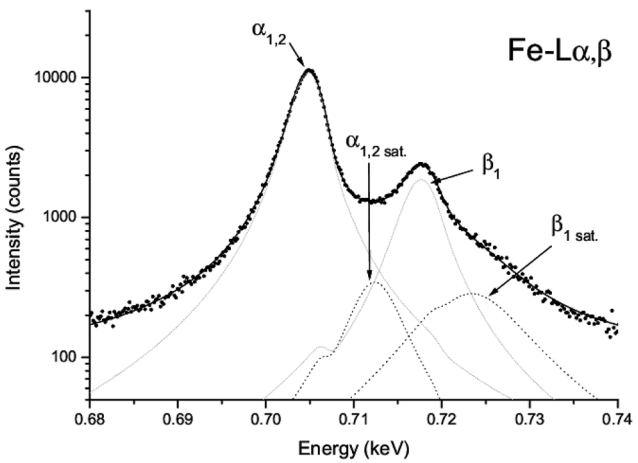

Fig. 8 X-ray spectrum of Fe in the Lα, Lβ$_1$ region. Dots: experimental spectrum; solid line: spectral fitting; dashed line: contribution of each diagram, satellite and RAE transition.

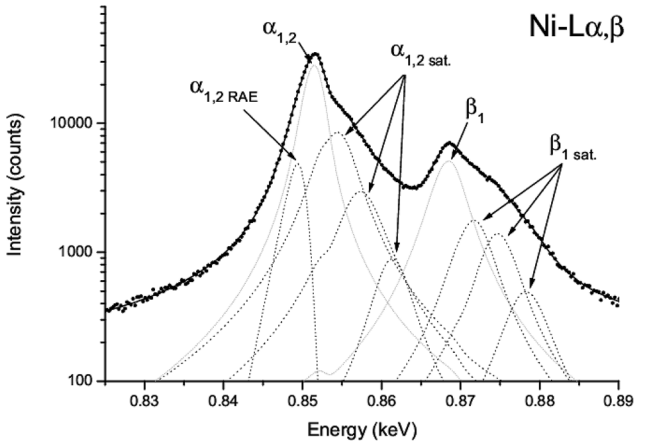

Fig. 9 X-ray spectrum of Ni in the Lα, Lβ$_1$ region. Dots: experimental spectrum; solid line: spectral fitting; dashed line: contribution of each diagram, satellite and RAE transition.

5 Conclusion

In the present work, the L lines of two 3d transition metals, Fe and Ni, were investigated. Besides the determination of diagram line energies, RTPs and natural linewidths, the satellite lines of both elements were studied, 2 of these transitions being determined for Fe and 9 for Ni. One of the latter was assigned to an $L_3M_{4,5}M_{4,5}$ RAE process. The robustness of the spectral processing method used allowed a detailed description of complicated structures, bearing in mind that the analyzed spectra were measured with a commercial wavelength dispersive spectrometer.

Regarding characteristic energies, the obtained data are in good agreement with other experimental results, except for the L_1M_2 and L_1M_3 lines, which in previous experimental studies were reported as doublets, whereas here they were determined separately.

Experimental data for L-line relative transition probabilities could not be found in the literature for the studied elements. For this reason, the RTP values obtained here were compared with theoretical calculations and interpolations, resulting in a better agreement with the former.

The natural linewidth values reported in this work were compared with the ones obtained from adding the energy level widths involved in each transition. However, this was not possible for the $L_3M_{4,5}$ and L_2M_4 lines, because the M_4 and M_5 level widths are not available in the literature. The degree of agreement is reasonable in most cases; nevertheless, the linewidth found for the L_1M_2 decay is much greater than that obtained by merely adding level widths. This fact suggests that in the emission spectrum this structure is complex and involves effects not accounted for by the theory nor appearing in the X-ray photoelectron spectroscopy spectra used to determine level widths.

Three satellite lines not previously reported, associated with the L_3M_1, L_2M_1 and L_2M_4 transitions, and a RAE structure were found for Ni. For both elements, all satellite intensities

obtained in this work, relative to their corresponding parent lines, could not be compared with any other previous result.

Finally, it is worth mentioning that a realistic description of the spectra was possible by means of the line profile introduced here to account for the differential attenuation at both sides of the absorption edge. It must be noticed that, because of the great number of structures associated with each diagram line, a reliable spectral processing is crucial to identify a reasonable number of peaks, consistent with the natural linewidths involved and with the instrumental resolution.

Acknowledgements

This work was financially supported by the Secretaría de Ciencia y Técnica (Universidad Nacional de Córdoba). The authors are also grateful to the Laboratorio de Microscopía Electrónica y Análisis por Rayos X (LAMARX) of the Universidad Nacional de Córdoba, Argentina, where the experimental determinations were performed.

References

1 J. A. Bearden, *Rev. Mod. Phys.*, 1967, **39**, 78.
2 Y. Cauchois and C. Sénémaud, *Wavelengths of X-ray Emission Lines and Absorption Edges*, Pergamon Press, 1978.
3 P. Indelicato, S. Boucand and E. Lindroth, *Eur. Phys. J. D*, 1998, **3**, 24–41.
4 R. D. Deslattes, E. G. Kessler Jr, P. Indelicato, L. de Billy, E. Lindroth and J. Anton, *Rev. Mod. Phys.*, 2003, **75**, 35–99.
5 J. H. Scofield, *Phys. Rev. A*, 1974, **10**, 1507.
6 S. T. Perkins, D. E. Cullen, M. H. Chen, J. H. Hubbell, J. Rathkopf and J. H. Scofield, *Tables and Graphs of Atomic Subshell and Relaxation Data Derived from the LLNL Evaluated Atomic Data Library (EADL), Z=1-100, Lawrence Livermore National Laboratory Report*, 1991, vol. 30.
7 J. L. Campbell and T. Papp, *At. Data Nucl. Data Tables*, 2001, **77**, 1.
8 R. Bonetto, G. Castellano and J. Trincavelli, *X-Ray Spectrom.*, 2001, **30**, 313.
9 S. Limandri, J. Trincavelli, R. Bonetto and A. Carreras, *Phys. Rev. A*, 2008, **78**, 022518.
10 P. Pérez, A. Sepúlveda, G. Castellano and J. Trincavelli, *Phys. Rev. A*, 2015, **92**, 062708.
11 F. Salvat, J. M. Fernández-Varea and J. Sempau, *OECD/NEA Data Bank*, Paris, Issy-les-Moulineaux, 2011.
12 S. Limandri, M. Vasconcellos, R. Hinrichs and J. Trincavelli, *Phys. Rev. A*, 2012, **86**, 042701.
13 R. D. Bonetto, A. C. Carreras, J. C. Trincavelli and G. E. Castellano, *J. Phys. B: At., Mol. Opt. Phys.*, 2004, **37**, 1477.
14 S. Limandri, R. Bonetto, H. Di Rocco and J. Trincavelli, *Spectrochim. Acta, Part B*, 2008, **63**, 962–967.
15 C. Fournier, C. Merlet, O. Dungne and M. Fialin, *J. Anal. At. Spectrom.*, 1999, **14**, 381–386.
16 G. Rémond, R. Myklebust, M. Fialin, C. Nockolds, M. Phillips and C. R. Carmes, *J. Res. Natl. Inst. Stand. Technol.*, 2002, **107**, 509–529.
17 H. Enkisch, C. Sternemann, M. Paulus, M. Volmer and W. Schülke, *Phys. Rev. A*, 2004, **70**, 022508.
18 T. Rodríguez, A. Sepúlveda, A. Carreras, G. Castellano and J. Trincavelli, *J. Anal. At. Spectrom.*, 2016, **31**, 780–789.
19 F. de Groot, *Coord. Chem. Rev.*, 2005, **249**, 31–63.
20 J. A. Bearden and A. F. Burr, *Rev. Mod. Phys.*, 1967, **39**, 125–142.

